Title
Evaluating the Uncertainties in the Shifts of Atmospheric Rivers (ARs) over Recent Decades in the Southern Hemisphere

Author
Shi, Zhan

Publication Date
2023

Peer reviewed|Thesis/dissertation

UNIVERSITY OF CALIFORNIA

Los Angeles

Evaluating the Uncertainties in the Shifts of Atmospheric Rivers (ARs) over Recent Decades in the Southern Hemisphere

A thesis submitted in partial satisfaction of the requirements for the degree

Master of Science in Atmospheric and Oceanic Sciences

by

Zhan Shi

2023

ABSTRACT OF THE THESIS

Evaluating the Uncertainties in the Shifts of Atmospheric Rivers (ARs) over Recent Decades in the Southern Hemisphere

by

Zhan Shi

Master of Science in Atmospheric and Oceanic Sciences

University of California, Los Angeles, 2023

Professor Gang Chen, Chair

In this study, we investigate the uncertainties mainly in the trends of frequency and shifts of ARs on the choice of AR detection algorithm and reanalysis data, and also analyze the causes of trends at various temporal and spatial scales using two ensembles from Community Earth System Model (CESM) simulations and decomposition covering the period of 1980-2016. Meteorological reanalyses show all-seasonal poleward shifts over the Pacific, in contrast to statistically insignificant equatorward shifts during MAM and SON over the Atlantic and Indian Ocean sectors throughout decades. The spatial patterns of intensification and shifts of ARs are largely driven by the changes in atmospheric circulation while anthropogenic forcing enhances the increase in moisture-driven AR frequency with nearly uniform warming over the Southern Ocean. Sea surface temperature (SST) variability characterized by the negative phase of the Interdecadal Pacific Oscillation (IPO) could generate dynamically-driven patterns of ARs to compensate for the poleward shift driven by thermodynamics.

The thesis of Zhan Shi is approved.

Rong Fu

Jonathan Lloyd Mitchell

Gang Chen, Committee Chair

University of California, Los Angeles

2023

TABLE OF CONTENTS

ACKNOWLEDGEMENTS

The meteorological data in the reanalysis datasets and Community Earth System Model (CESM) model simulations were prepared and provided by Weiming Ma of UCLA (now postdoc of the Pacific Northwest National Laboratory) and gratefully acknowledged. Comments and suggestions by Gang Chen, Jonathan Mitchell, and Rong Fu of UCLA, Department of Atmospheric and Oceanic Sciences were appreciated.

1. Introduction

Atmospheric river (AR) is defined as a long, narrow and transient corridor of strong integrated horizontal water vapor transport (IVT) in the lower troposphere, typically featured by highly-concentrated moisture and low-level jet stream ahead of the cold front of an extratropical cyclone (Rutz et al., 2019; Payne et al., 2020; Zhou & O' Brien et al., 2021; Zhang, Ralph & Zheng, 2019). ARs are important components of the meridional transport of atmospheric moisture resulting in over 90% of the poleward moisture transport at midlatitudes (Zhu & Newell, 1998). With intense moisture transport, ARs generate forced precipitation through interaction with topography or ascent along a warm conveyor belt or frontal boundary (Payne et al., 2020). AR precipitation is positively correlated with IVT, regarded as AR intensity (Rutz et al., 2014). AR events are associated with about 40-75% of extreme wind and precipitation at 40% of the world's coastlines in mid-latitude ocean basins (Waliser & Guan, 2017). In California, ARs have been historically contributing to water supplies but also have caused substantial socio-economic damage from landslides and flooding by generating extreme precipitation which challenges water resource management (Payne et al., 2020; Michaelis et al., 2022; Swain et al., 2018; Gershunov et al., 2017; Dettinger et al., 2011; Guan et al., 2010). In California, precipitation and streamflow totals, generally fueled by landfalling ARs on the west coast, have large annual variations due to large storms, and AR-driven precipitation contributes 20 - 50% of the state's precipitation (Michaelis et al., 2022; Dettinger et al., 2011). ARs also extend into the polar regions and further disturb the sensitive feedback processes (Nash et al., 2018). While ARs and associated extreme water vapor transport rarely occur over the polar regions, studies show that 40-60% of the total annual precipitation in certain Antarctic regions is from the top 10% of extreme daily precipitation events (Turner et al., 2019). ARs contribute

significantly, around 13%, to the Antarctic accumulated snowfall (10-20% of the total snowfall across East Antarctica) and a majority of extreme precipitation events across the middle to high latitudes where ARs mostly occur (Wille et al., 2021). In addition, ARs also control the mass balance by triggering ice melting or amplifying warming by affecting the surface radiative balance and generating condensational latent heat or turbulent heat fluxes (Francis et al., 2020; Wille et al., 2019; Komatsu et al., 2018). Studies show that ARs influence the decline of Arctic sea ice (Hegyi & Taylor, 2018) and result in short-duration but high-volume surface melting events, particularly in West Antarctica (Maclennan et al., 2022).

The changes in ARs can be decomposed into contributions from atmospheric moisture variability caused by thermodynamic processes, and changes in the atmospheric circulation that transports water vapor driven by large-scale atmospheric circulation (Ma et al., 2020). Different aspects of water vapor transport in individual AR events are further distinguished into “wet” (moisture-dominated IVT) and “windy” (wind-dominated IVT). Windy ARs modulate the precipitation magnitudes and generate greater precipitation, particularly over orography and at higher IVT. As the global mean surface temperature increases, the water-holding capacity of the atmosphere will be enhanced which helps intensify the moisture transport, thus strengthening the moisture dominance of regional ARs (Algarra et al., 2020; Gonzales et al, 2020). The intensity of AR-driven precipitation and hydrological extremes will also be enhanced by increased atmospheric moisture following Clausius–Clapeyron scaling in which the column-averaged integrated moisture increases at a rate of 7.3%/k with respect to the average surface air temperature (Payne et al., 2020; Allan, 2012; O’Gorman & Muller, 2010). In CMIP5/6 future simulations, most AR detectors indicate a global increase in AR frequency, sizes, and counts with strong radiative forcing (O’Brien et al., 2021). AR activities are also modulated by

large-scale dynamics characterized by diverse intensities, moisture sources, and preferred tracks of future ARs with climate change (Payne et al., 2020; Fish et al., 2019). In the tropics, ARs in the North Pacific region are affected by the Madden-Julian oscillation (MJO), convectively coupled equatorial waves, the quasi-biennial oscillation, and El Nino-Southern Oscillation (Benedict et al., 2019). In the extratropics, shifts in the North Pacific upper-tropospheric jet stream associated with Rossby wave propagation and Rossby wave breaking can significantly modulate AR intensity and landfall location (Payne & Magnusdottir, 2014; Neiman et al., 2008). Rossby wave breaking dynamically influences the AR moisture dominance as well (Gonzales et al, 2020; Benedict et al., 2019; Mundhenk et al., 2016). Investigation of ARs in the Southern Hemisphere is still an area of ongoing research (Ma et al., 2020).

Due to the dependency on identification algorithms and the complexity of their evolution, the identification and characterization of ARs in large datasets including reanalyses and climate simulations remain uncertain (Michaelis et al., 2022), so a collection of identification and tracking methods have been developed, termed Atmospheric river detection tools (ARDTs). ARDTs are applied to objectively and quantitatively discriminate ARs, normally featured by anomalously high moisture or moisture transport that occurs in continuous and filamentary structures from the background in the datasets by following a set of thresholds and filters (O'Brien et al., 2022). Recently, the Atmospheric River Tracking Intercomparison Project (ARTMIP), which has so far worked on tier 1 and 2 experiments, is an international effort initiated by the U.S. Department of Energy (DOE) and National Oceanic and Atmospheric Administration (NOAA) scientists to systematically understand and quantify the uncertainties in AR science based on the choice of methodology (Tier 1) and describe the impacts on climate science and other fields (Tier 2) (Payne et al., 2020; Shields et al., 2018). Shields [2019] found

that the climatology of ARs (e.g. the frequency, duration, intensity, propagation speed and predictability) largely depends on the choice of ARDTs. The occurrence of consensus ARs concentrates on the extratropics while the largest disagreement between the global detection methodologies results from the detection of weak features (Lora et al., 2020). High-resolution historical and future climate model simulations illustrate that uncertainties in projected AR frequency and AR-driven precipitation are sensitive to ARDT selection (Shields et al., 2023; O'Brien et al., 2022). Zhou and O'Brien [2021] studied and found common AR-MJO and AR-ENSO connections across different AR detection methods since responses of AR to climate change are tied to the definition of the feature. Although the detector-related uncertainties may be negligible at a time scale longer than AR itself, there're still large disagreements in the regional AR-related research, indicating more challenges need to be overcome regarding how AR responds to different modes of climate variability. Intercomparison of algorithms enables further understanding of the underlying physical processes (e.g. transient baroclinic instabilities) that influence the evolution of ARs during their life cycles and features ("flavors") associated with ARs observed across various classes of AR algorithms which is the main source of challenges for the categorization of ARDTs (O'Brien et al., 2020). Understanding the disagreements and developmental intent of the ARDTs will also affect the choice of ARDTs for different purposes when applying to different scientific questions (e.g. with diverse geographical or topographical constraints, or different horizontal resolutions) (Shields et al., 2023; Collow et al., 2022; O'Brien et al., 2022). Moreover, it is helpful for the stakeholder communities to better know their socio-economic impacts such as assessment of hazards (e.g. extreme precipitation, floods, and storms), water management, city and transportation planning, agriculture or industry that relies on global and regional hydrological information (Shields et al., 2019).

Based on both observations and climate models, there has been a meridional shift of westerly jets in the Southern Hemisphere over the past few decades (Waugh et al., 2020; Swart et al., 2015; Solman & Orlanski, 2014; Chen & Held, 2007; Kushner et al., 2001; Yang et al., 2020). Waugh [2020] analyzed the intensification and shift of regionally averaged winds. Thomas [2015] analyzed the natural variability of extratropical circulation by comparing Coupled Model Intercomparison Project Phase 5 (CMIP5) preindustrial control model runs and observed trends in Southern Annular Mode (SAM), jet magnitude, and location that are all related to changes in ocean circulation, and found that those trends could be due to the combination of natural variability and external forcing. Swart [2015] found the spatial structure of the observed trends in zonal winds largest, but also most uncertain in the southeastern Pacific. The mean trend in the CMIP5 is similar to observations in the core area of the westerlies while several reanalyses overestimate the recent trends (Swart et al., 2015). AR events usually occur in conjunction with the strong low-level wind like westerly jets, according to the definition of IVT, but strong surface wind associated with AR has been less discussed in the AR literature compared with AR-driven precipitation (Gonzales et al., 2020). Understanding the physical (i.e. dynamic and thermodynamic) processes associated with ARs is very crucial in the context of climate change. Ma [2020] investigated the trend of annual ARs over the Southern Ocean over recent decades and found the majority of AR frequency trends are driven by large-scale atmospheric circulation. The results show an increase in AR frequency over the Southern Ocean and a decrease over lower latitudes in the past four decades which generate poleward AR shifts. Fully coupled CESM experiments indicate evidence of positive AR frequency trends driven by anthropogenic forcing and dynamically-driven trends forced by observed sea surface temperature that reconcile the moisture-driven trends. In this study, we aim to further study the seasonal changes of ARs and

decomposed components driven by dynamics and thermodynamics over individual ocean basins to investigate the impacts of external forcing, and also intercomparison among the identification methods and reanalyses to quantify the uncertainties in the choice of method and data. The remainder of this manuscript is organized into five sections. Section 2 includes the description of data sets and methods used in this study. Section 3 includes the discussion and analysis of results which are concluded in section 4.

2. Data and Methods

2.1 Observation and Climate model

For the analysis of different observation, we use five reanalyses between 1980 - 2016, including the ECMWF global atmospheric reanalysis ERA-Interim which provides global, 6-hourly atmospheric fields at 1.5°×1.5° spatial resolution and the fifth generation ECMWF global atmospheric reanalysis (ERA5) at the higher spatial resolution of 1°×1°, version 2 of the National Aeronautics and Space Administration (NOSA) Modern-Era Retrospective analysis for Research and Applications, Version 2 (MERRA-2) at the horizontal spatial resolution of 0.5°×0.625°, National Centers for Environmental Protection-National Center for Atmospheric Research (NCEP-NCAR) Reanalysis Project at the NOAA Physical Sciences Laboratory at the horizontal spatial resolution of 2.5°×2.5°, and the Japanese 55-year Reanalysis (JRA55) at the horizontal spatial resolution of 1.25°×1.25°. Calculations of IVT from reanalyses use data at 00:00 UTC each day (no impacts on results if use mean values). The AR detection developed by Guan and Waliser et al., (2015) uses a fixed threshold for integrated water vapor transport (IVT) that derives from horizontal wind and specific humidity at pressure levels between surface and 200mba pressure level (near surface level, 850mba, 500mba, 200mba in the reanalysis except

that 300mba is the highest level in NCEP-NCAR due to lack of pleasure data above 300 mba) (see equation below).

$$IVT = [(\frac{1}{g}\int_{surface}^{200mba} qu\, dp)^2 + (\frac{1}{g}\int_{surface}^{200mba} qv\, dp)^2]$$

Where g is the acceleration due to gravity, q is the specific humidity; u and v are the zonal and meridional layer-averaged wind; dp is the pressure increment between two successive pressure levels.

We also use daily mean values from two ensembles of CESM simulations at a spatial resolution of 0.9°×1.25°. We use the 40-member fully coupled atmosphere-ocean simulations from the CESM Lapse Ensemble (LENS) (Kay et al., 2015). The ensemble is forced by the observed historical forcing from 1920 to 2005 and Representative Concentration Pathway 8.5 (RCP8.5) forcing since 2006 which will be a good approximation of the reality for 2005 to 2020 if look at the total cumulative carbon dioxide (CO2) emission during that period. (Moss et al., 2010; Taylor et al., 2012; Ma et al., 2020). The other one is a 10-member atmosphere-only ensemble from the same version of CESM, Version 1.1 (GOGA). They use the same historical forcing as LENS (except the ozone forcing) followed by applying time-varying prescribed National Oceanic and Atmospheric Administration (NOAA) Extended Reconstruction Sea Surface Temperature (SST), Version 4, and Hadley Centre Sea Ice. In spite of the likelihood of underestimating the dynamic contribution to AR frequency trends in GOGA due to slightly difference in forcing (Schneider and Deser et al., 2018; Ma et al., 2020), another study shows that it has statistically insignificant effects on the trends of the westerly jet in Southern Hemisphere during the satellite era and thus would not affect the conclusion in this study. Each ensemble member only differs in the initial condition by applying a small perturbation in initial

atmospheric temperature fields.

2.2 AR detection algorithms

To facilitate the intercomparison of ARDTs, 8 different ARTMIP methods are included and 3-hourly IVT in MERRA2 is aggregated as shown in Table 1.

Table 1
List of Selected AR Detection Algorithms

No.	ARDT	Reference	Region	Thresholds
1	Cascade_bard_v1	O'Brien et al. (2020)	Global	Relative threshold (based on spatial percentile for each timestep). An inverted Gaussian filter is applied at the equator to damp out the ITCZ.
2	Lora_global	Lora et al. (2017)	Global	Length ≥ 2,000 km; IVT anomaly ≥ 100 $kg\ m^{-1}\ s^{-1}$ by subtracting climatological and regional mean IVT from the daily IVT field
3	Guan_waliser	Guan and Waliser (2015)	Global	Relative: 85^{th} percentile IVT; Absolute min requirement designed for polar locations: 100 $kg\ m^{-1}s^{-1}$ IVT
4	Mundhenk_v3	Mundhenk et al. (2016)	Global	IVT anomaly ≥ 250 $kg\ m^{-1}s^{-1}$ by subtracting climatological mean and seasonal cycle
5	ClimateNet	Kashinath et al. (2020)	Global	Threshold free; input fields are IWV, U850, V850, SLP
6	PanLu	Pan and Lu (2019); Pan and Lu (2020)	East Asia & Global but latitude ≥ 15°N	Length ＞2000 km; length-width ratio exceeds 2; sum of turning angle < 360°; exceed local threshold (85% quantile IVT) and regional threshold (80% quantile IVT in the detection region)
7	Tempest_ivt250	Ullrich & Zarzycki (2017); McClenny et al. (2020); Rhoades, Jones, O'Brien et al. (2020)	Global but latitude ≥ 15°N	∇^2IVT ≤ -5e4 $kg\ m^{-1}s^{-1}\ rad^{-2}$, IVT ≥ 250 $kg\ m^{-1}s^{-1}$; object ＞25 grid points
8	CASCADE_IWV	Experimental	Global	Convolutional neural network to

				replicate ARTMIP mean; Threshold free; use IWV as input

2.3 Dynamic and Thermodynamic Decomposition

A scaling method to decompose the dynamic and thermodynamic contributions to the AR frequency trends in this study is developed by removing the interannual variability of the annual mean specific humidity (Ma et al., 2020). The AR frequency derived from the scaled IVT (i.e. dynamically-driven specific humidity, q_{dynam}u, see equation below) indicates the dynamic component of the total AR frequency, while the corresponding linear trends represent the AR frequency trends driven by atmospheric dynamics, and the difference represents thermodynamically-driven trends.

$$q_{dynam} = q_{i,j} \times q_c / q_m$$

Where q_c is the climatological specific humidity at the level at each grid cell, q_m is the annual mean specific humidity at the same level at each grid cell in the given year. Climatological specific humidity is calculated by averaging the data of the study period.

2.4 Latitude of ARs

The averaged latitude of ARs is weighted by AR frequency and area at particular latitudes between 20°S - 60°S in order to zoom into the mid-latitude regions. The calculation of area-weighted mean latitude is shown by the equation:

$$Area - weighted\ AR\ frequency\text{: } wf(i) = f(i) * cos(\frac{lat(i)}{\pi})$$

$$lat(i) \subset [-60, -20],\ i\ represents\ the\ index\ of\ latitude$$

Where lat represents the vector of latitudes (degrees in the meridional direction), while wf(i), f(i) and lat(i) indicate the value at particular latitude using the index i. f(i) represents the zonally averaged AR frequency within each ocean basin.

$$Area - weighted\ mean\ latitude\ of\ ARs\colon\ wl(i) = \sum_{-20°}^{-60°} \left[\frac{lat(i) * wf(i)}{\sum_{-20°} wf(i)}\right]$$

The method to calculate the centroid latitude of AR events is developed by Guan and Waliser (2015), but not used in this study. However, the conclusions in this study will not be affected by the use of the method.

3. Results

3.1. Intercomparison of the AR Detection Algorithms

AR frequency is the most basic attribute characterizing the climatology of ARs of which the global distribution represents the fraction of time during which AR conditions occur at any given location. Figure 1 shows the distributions of seasonal AR frequency (MAM: March - May; JJA: Jun - Aug; SON: Sep - Nov; DJF: Dec - Feb) in the Southern Hemisphere from 8 AR detection algorithms during 1980-2016. It presents uncertainties in the AR frequency detected by different ARDTs and shows spatial patterns of AR frequency roughly coincide with the storm tracks (Shaw et al., 2016). AR frequency has different magnitudes based on the choice of ARDT, but all the spatial distributions present large magnitudes of AR frequency clustering over the extratropical oceans which are in agreement with the results by Lora et al. (2020), Collow et al. (2022) and other findings from ARTMIP. AR total trends vary among seasons characterized by positive signals (i.e. increasing trends) covering large areas, particularly the extratropics, and several areas of negative signals (i.e. decreasing trends) while some of the seasonal trends are

very noisy, like Guan_Waliser. The magnitude of seasonal trends differs among ARDTs. For example, Tempest250 and CASCADE_IWV have smaller areas of strong positive trends compared with ClimateNet and PanLu.

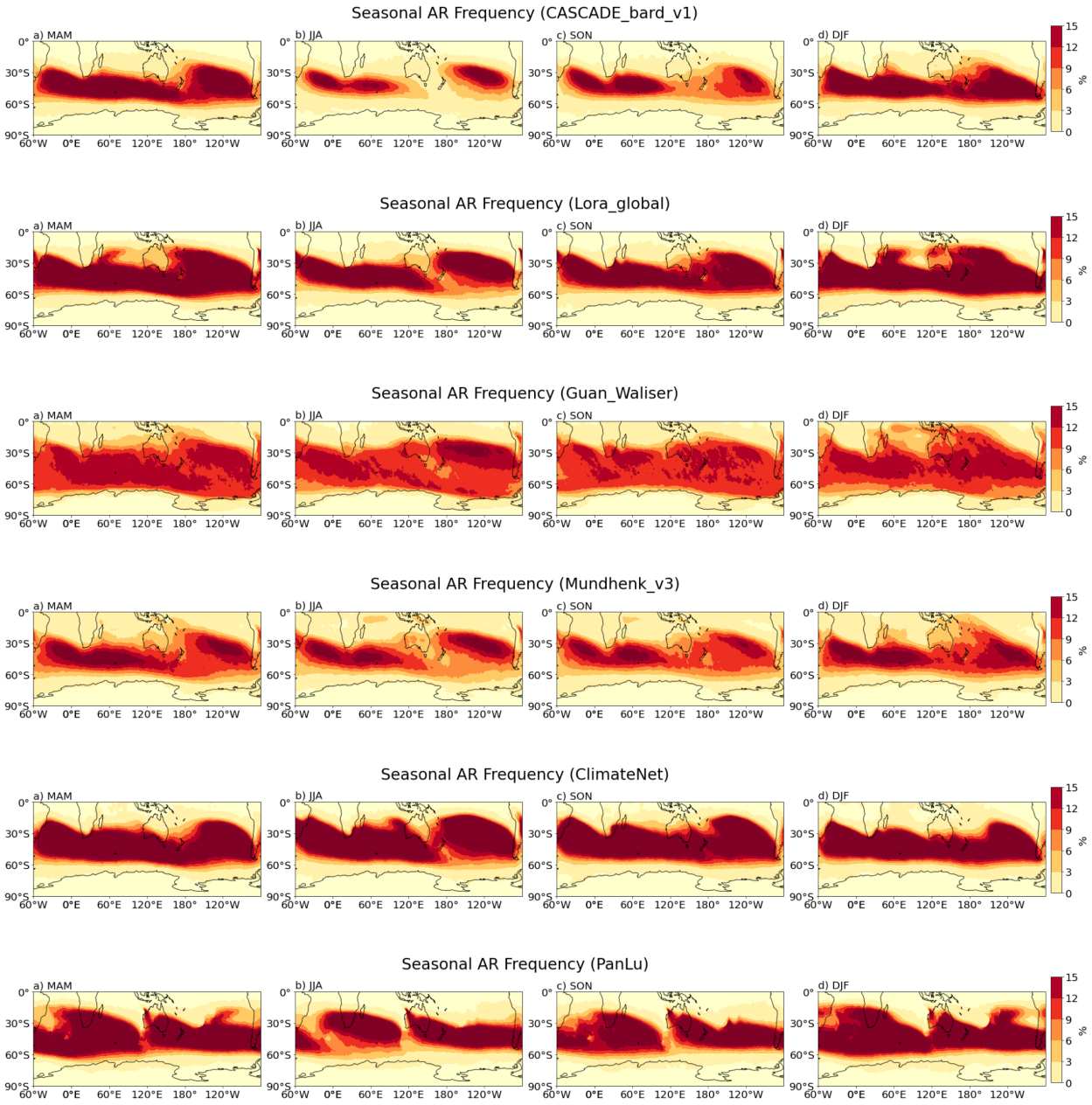

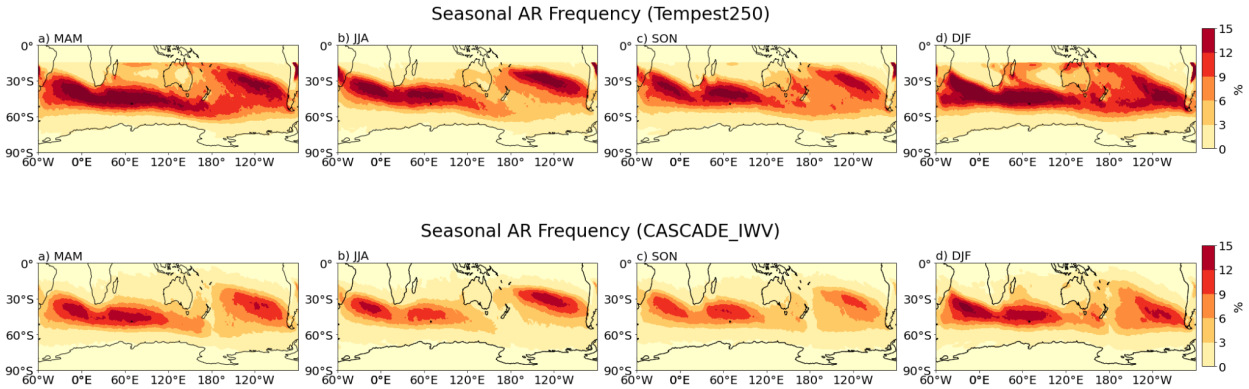

Figure 1. Spatial distribution of climatological (shading) seasonal AR frequency identified by 8 AR detection algorithms based on Modern-Era Retrospective analysis for Research and Applications, Version 2 (MERRA2): Cascade_bard_v1, Lora_global, Guan_waliser, Mundhenk_v3, ClimateNet, PanLu, Tempest_ivt250, CASCADE_IWV. AR frequency is defined as the fraction of time during which AR conditions occur at any given location annually or seasonally of which the magnitude is represented by shadings. Coastlines are shown in black.

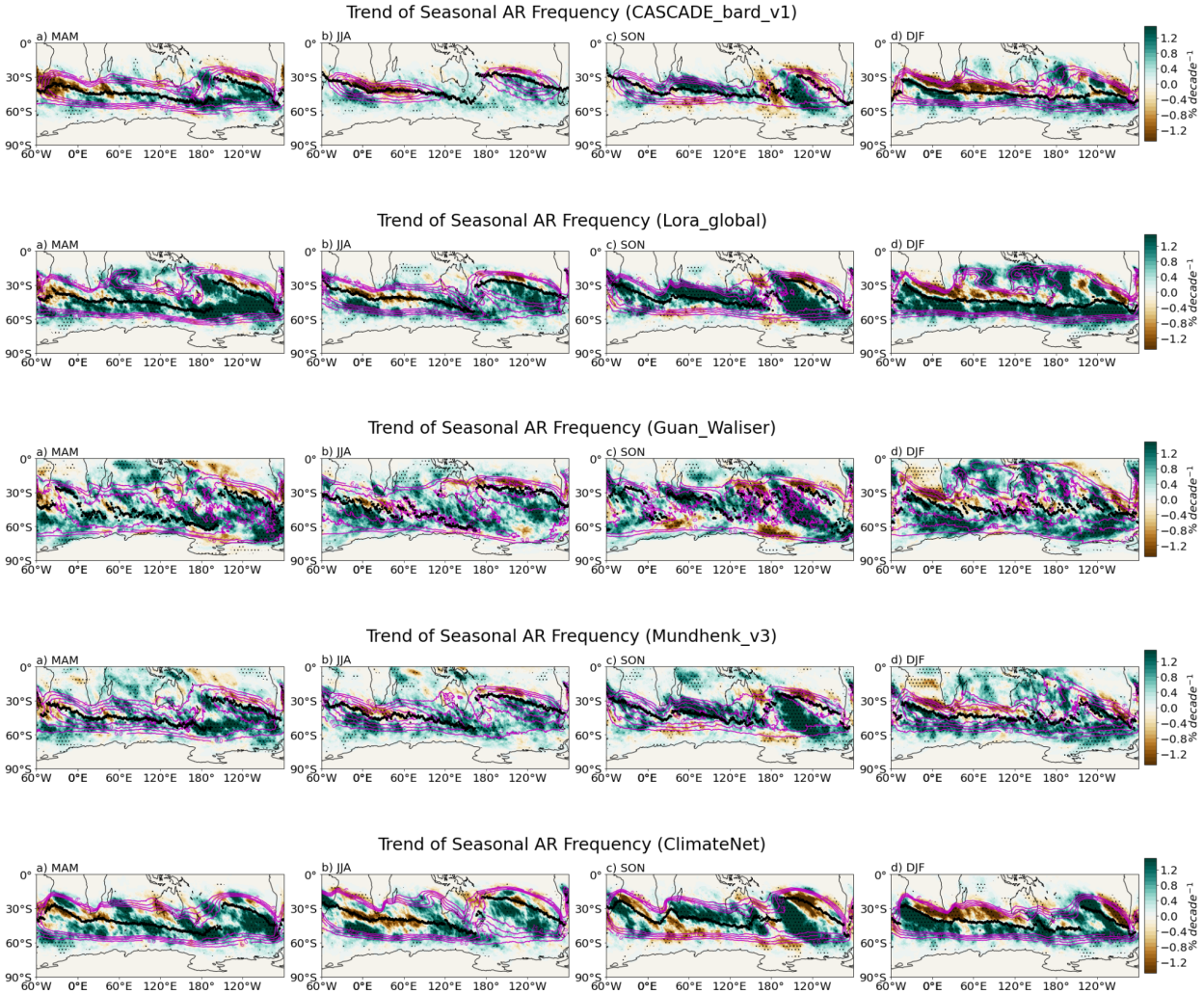

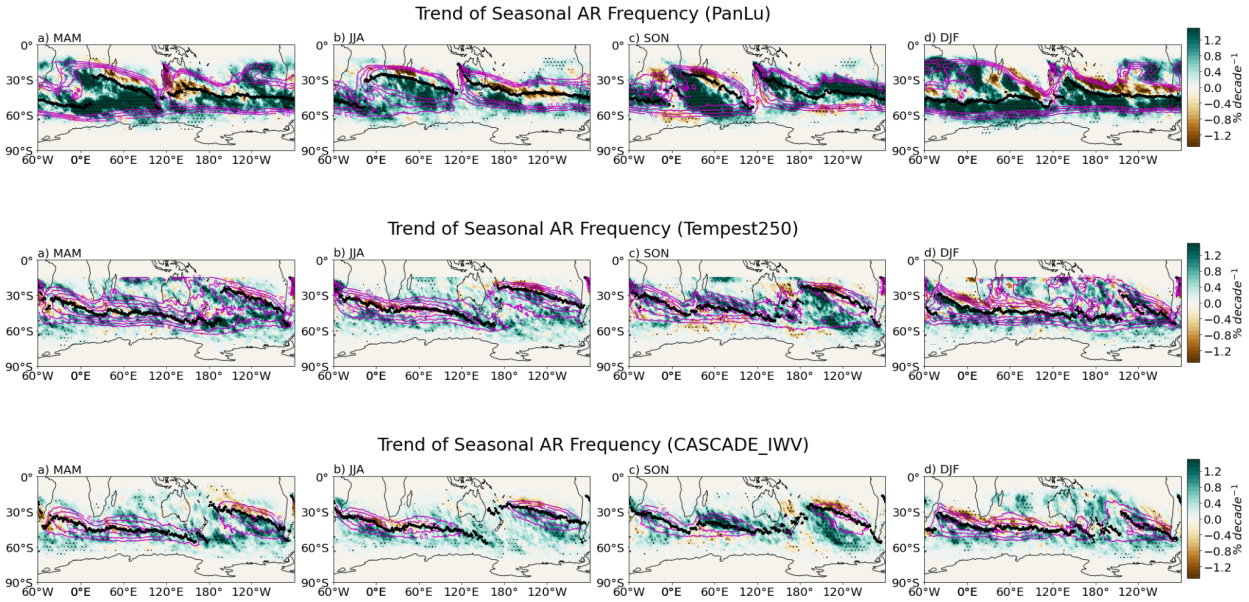

Figure 2. Spatial distribution of climatology (contours) and the linear trends (shading, % $decade^{-1}$) of seasonal AR frequency identified by 8 AR detection algorithms based on Modern-Era Retrospective analysis for Research and Applications, Version 2 (MERRA2): Cascade_bard_v1, Lora_global, Guan_waliser, Mundhenk_v3, ClimateNet, PanLu, Tempest_ivt250, CASCADE_IWV. Coastlines are shown in black. Black line indicates the climatological location of peak AR frequency. Stippling indicates regions with trends significant at the 90% significance level based on two-tailed Student's t test.

The area-weighted latitudes of annual and seasonal ARs are used to calculate the shift of ARs at different spatial scales (i.e. within the whole Southern Ocean (SH) and individual ocean basins, such as Pacific(PA), Atlantic and Indian Ocean sectors (ATIN)), as shown in Figure 3. There're large spreads in the shifts through the application of different ARDTs. Over the Southern Ocean, there is a poleward shift of annual ARs, except for PanLu, at an average rate of -0.13°±0.079° latitude per decade. The seasonal ARs in the Southern Ocean show poleward shifts at an average rate of -0.22°±0.095° latitude per decade in JJA, but also statistically insignificant equatorward shifts during SON. While ARs in the Pacific shift poleward in all seasons, the smallest shifts usually occur in DJF at an average rate of -0.17°±0.081° latitude per decade and the largest occur in MAM, JJA, and SON ranging from -0.2° ~ -0.6° latitude per decade (Figure 3b). ARs over the Atlantic and Indian Ocean sectors detected by some selected ARDTs have prominent, but

statistically insignificant equatorward shifts in MAM and SON at an average rate of 0.04°±0.12°, 0.20°±0.14° latitude per decade, and poleward shifts in DJF and JJA at a rate of -0.16°±0.075°, -0.15°±0.082° latitude per decade (Figure 3c).

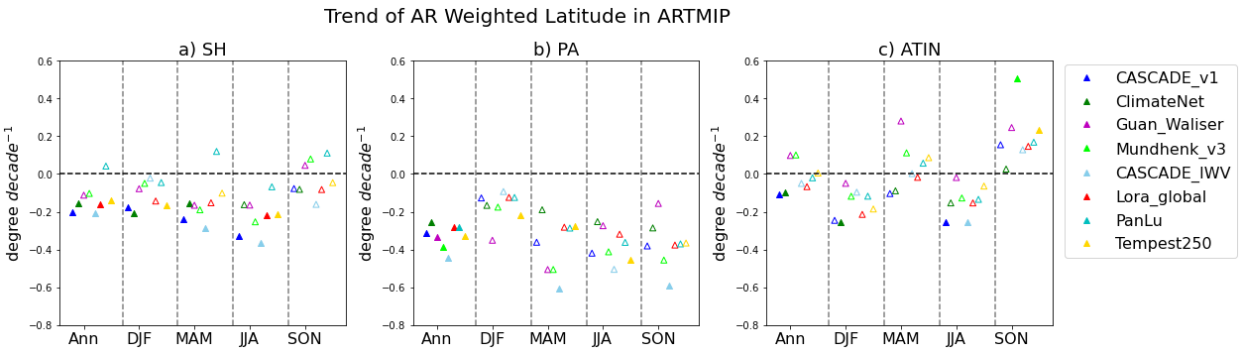

Figure 3. Linear trends of annual and seasonal AR area-weighted latitudes over: a) Southern Hemisphere (SH), b) Pacific Ocean basin, c) Atlantic and Indian Ocean sectors. AR frequency are identified by 8 algorithms shown with triangles in different colors: Cascade_bard_v1, Lora_global, Guan_waliser, Mundhenk_v3, ClimateNet, PanLu, Tempest_ivt250, CASCADE_IWV. Solid triangles represent the trends significant at the 95% significance level based on P-value.

3.2. Trends of Atmospheric River (AR) frequency in the Southern Hemisphere

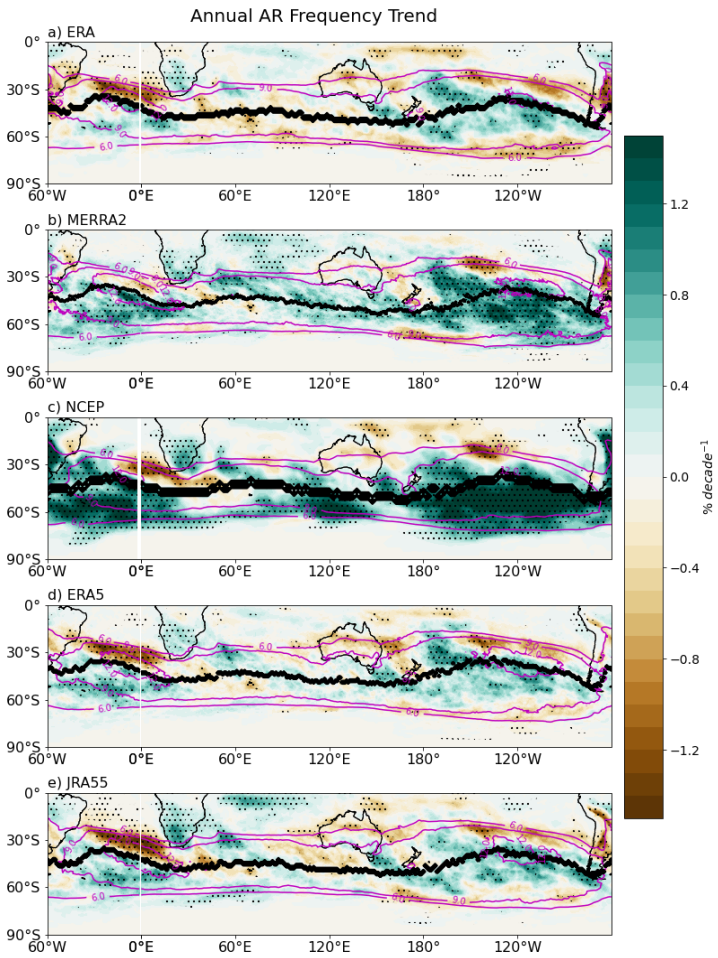

Figure 4. Spatial distribution of trends (solid contours) and linear trends (shading, % $decade^{-1}$) of annual AR frequency in ERA, MERRA2, NCEP, ERA5, JRA55. Black line indicates the climatological location of peak AR frequency. Coastlines are partially shown in black. Stippling indicates regions with trends significant at the 90% significance level based on two-tailed Student's t test.

Trends of annual AR frequency from different reanalysis data have different spatial patterns (Figure 4). All reanalysis datasets show stronger positive annual AR frequency trends over the Pacific compared to other ocean basins. Moreover, spatial distributions of annual AR frequency trends show a poleward shift of ARs with increasing AR frequency on the poleward side and decreasing AR frequency on the equatorward side of climatological locations of peak AR frequency. Changing occurrence of AR events may impact the local weather and climate such as

prolonged drought in Australia during El Niño and positive Indian Ocean Dipole (IOD) events (McKay et al., 2023), reduced rainfall, and even drought in central Chile (Fuentes et al., 2021; Boisier et al., 2016) and variability of sea-ice melting in Antarctica (Davison et al., 2023).

AR consists of both moisture and horizontal low-level winds which are strongly affected by the SST variability. To figure out the cause of AR frequency trends, Figure 5 presents the spatial distributions of seasonal AR frequency trends from observations (i.e. reanalysis mean) and ensembles of CESM simulations (GOGA and LENS). In the reanalysis, seasonal AR frequency trends in DJF and JJA have positive AR frequency trends on the southern flank of the climatological peak over the Atlantic and Indian Ocean sectors, producing poleward AR shifts (Figure 5, upper, b, d). The inverse pattern during SON drives equatorward AR shifts (Figure 5, upper, c). Over the Pacific, there are positive AR frequency trends during all seasons at extratropics. Analyzed by Ma et al. (2020), SST trends in LENS show relatively more uniform positive signals (i.e. warming pattern) in the Southern Hemisphere compared with GOGA in which the cooling region exists near the coast of Antarctica and tropics associated with warming in the subtropics (see their Figure 1). Therefore, observed SST variability in GOGA brings ensemble mean AR frequency trends in closer agreement with the observed trends featured by some negative trends (not all) on the northern side of the climatological peak ARs and near the west coast of Antarctica, especially during SON, and an extensive band of increased AR frequency over the Pacific reaching from northwestern/central to southeastern Pacific. AR frequency trends from ensemble mean of LENS which represent anthropogenically forced signals under the RCP 8.5 scenario are characterized by positive trends covering the majority of extratropical regions over the Southern Ocean that reveal rather a uniform warming pattern on the polar side of the climatological peak. In conclusion, anthropogenic forcing contributes a lot

to the positive trends in the Southern Ocean, and internal SST variability plays an important role in modulating the spatial pattern of ARs over the Southern Ocean that is similar to the observed.

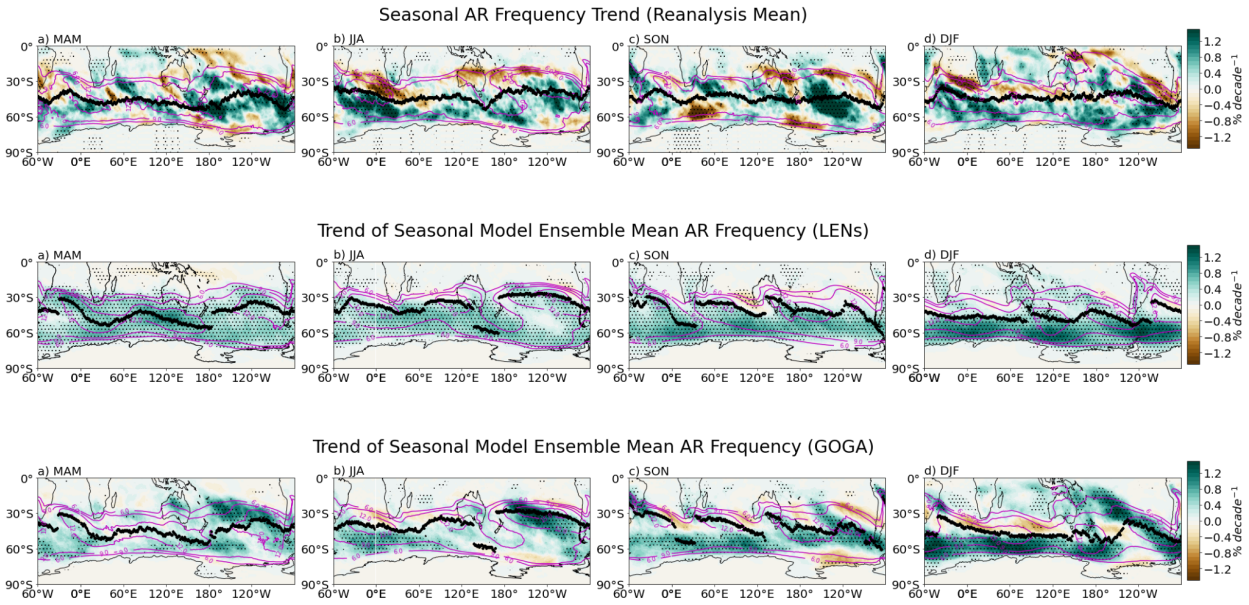

Figure 5. Spatial distribution of climatology (solid contours) and linear trends (shading, % $decade^{-1}$) of: seasonal reanalysis-mean AR frequency (upper panel), seasonal AR frequency in GOGA (middle panel), seasonal AR frequency in LENs (bottom panel). Black line indicates the climatological locations of peak AR frequency. Stippling indicates regions with trends significant at the 90% significance level based on two-tailed Student's t test.

3.3. Uncertainties in the Shifts of AR Frequency

To better illustrate the shifts of ARs over recent decades, trends of zonal mean AR frequency across the latitudes at smaller spatial and temporal scales are analyzed for understanding AR shifts (Figure 6). The magnitudes of zonal mean AR frequency trends normally peak on the poleward side of AR latitude, especially at high latitudes (<40°S). In comparison with other reanalyses, NCEP has the largest increasing trend in AR frequency at around 50°S ~ 60°S. The negative signals due to reduced AR frequency during SON at around 60°S south to the climatological location of peak AR frequency over the Atlantic and Indian Ocean sectors are

apparent in Figure 6, bottom. AR latitudes from model ensembles and reanalyses place further north during boreal summer and fall (JJA and SON) and shift southward during boreal winter and spring (DJF and MAM), as also captured by GOGA and LENs and similar to the seasonal changes in jet locations. The majority of trends from reanalysis data fall within the spread of models.

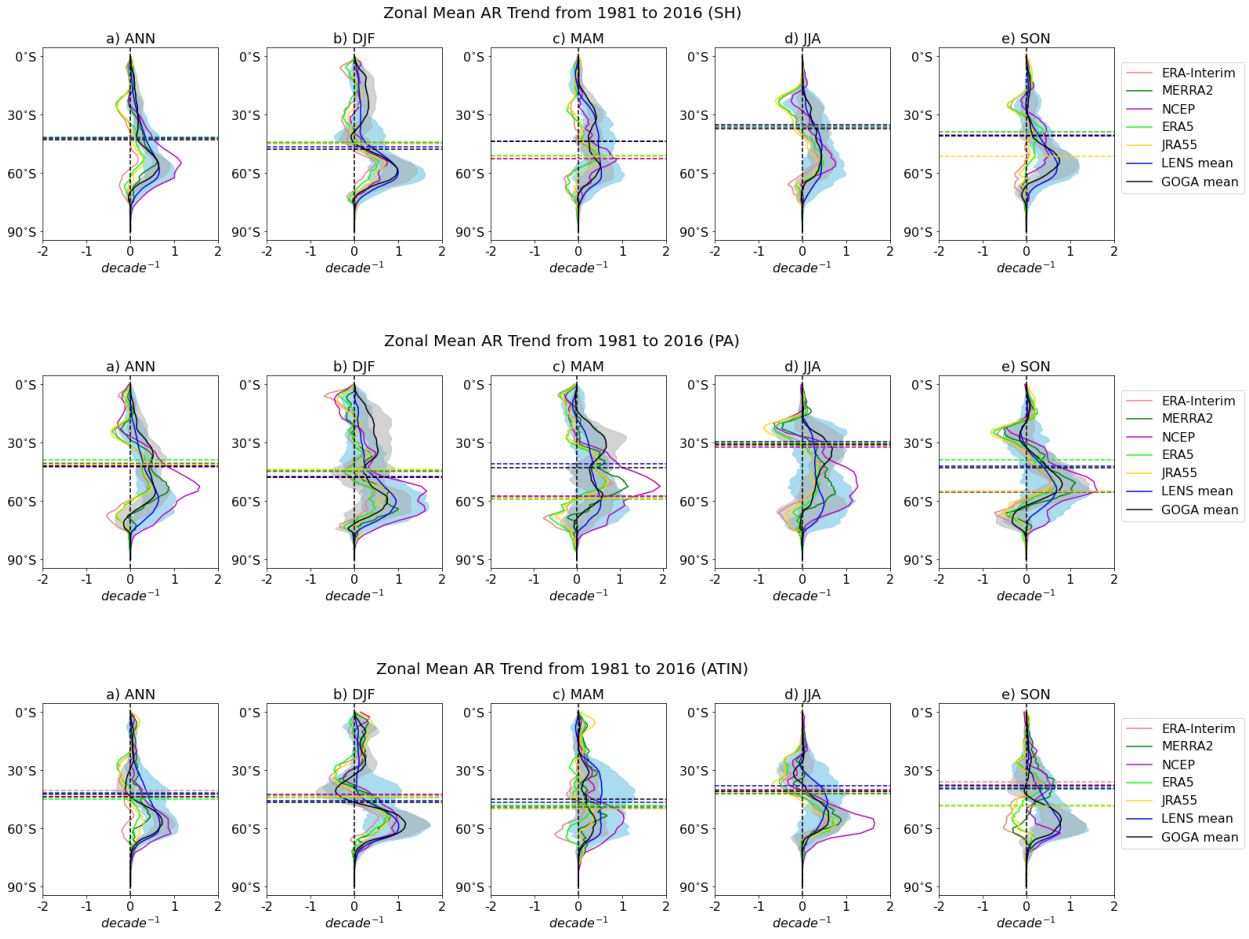

Figure 6. Linear trends of zonal seasonal AR frequency averaged over: Southern Hemisphere (SH; upper panel), Pacific Ocean basin (PA; middle panel), Atlantic and Indian Ocean sectors (ATIN; bottom panel). Horizontal lines indicate the climatological location of peak AR frequency and shadings indicate the spread in each model.

Consistent with the shifts of ARs using different ARDTs (Figure 3), the observed AR frequency presents statistically significant poleward shifts at an average rate of -0.38°±0.090° latitude per

decade in JJA while the smallest poleward shift occurs in SON at an average rate of -0.16°±0.050° latitude per decade over the Southern Ocean (Figure 7a). NCEP usually presents the largest poleward AR shift among all the reanalysis data. The seasonality of AR shift also varies in individual ocean basins (Figure 7b, c). Over the Pacific, AR shifts during the period of 1980 - 2016 are dominant with negative signals representing poleward shifts. The biggest shifts usually occur in SON (except NCEP) at an average rate of -0.49°±0.092° latitude per decade, and the smallest occur in DJF at an average rate of -0.18°±0.11° latitude per decade. Associated with the largest poleward shift in JJA at an average rate of -0.41°±0.10° latitude per decade over the Atlantic and Indian Ocean sectors, there is a slightly equatorward shift in SON (0.087°±0.061° latitude per decade) agreed among all the reanalysis data indicating a different characteristic of seasonal AR shifts in reanalyses over the ATIN though they're not statistically significant at 95% significance level (a P-value of 0.05 or 5%). That seasonal AR shifts of MERRA2 differ from ARTMIP results may be solely caused by 6-hourly and 3-hourly IVT that are used to define the AR. Considerable variability exists among the members of CESM ensembles in the magnitude and sign of the trends that also differ from the observations. Ensemble mean AR frequency trends averaged over all the members in GOGA present equatorward shifts in MAM in the SH; DJF, MAM, and JJA in the Pacific (Figure 7a, b). However, although GOGA shows consistent spatial patterns of AR frequency trends with the observations, both GOGA and LENS fail to reproduce the equatorward shift over the Atlantic and Indian Ocean sectors in SON which is probably caused by other physical processes that are not well reproduced in the model simulations (Figure 10). The influence of atmospheric teleconnection on ARs still needs further research. Studies show that models seem to vary in their ability to simulate the temporal variation of the teleconnection patterns and still need further

improvement in the simulation of wave-train-like atmospheric teleconnection patterns (Handorf & Dethloff, 2012; Cassado & Pastor, 2012; Stoner et al., 2009). The equatorward shifts during SON over the Atlantic and Indian Ocean sectors could probably be related to the equatorward shifts of westerly jets in the Southern Pacific during SON from ERA-Interim, JRA55, and MERRA-55 found by Waugh (2020) (see their Figure 3).

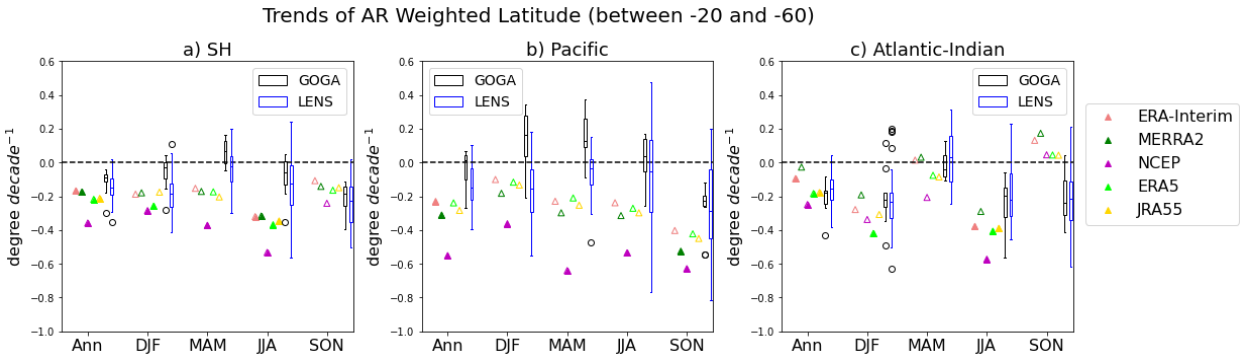

Figure 7. Linear trends of annual and seasonal AR area-weighted latitudes over: a) Southern Hemisphere (SH), b) Pacific Ocean basin (PA), c) Atlantic and Indian Ocean sectors (ATIN). Reanalyzed AR frequency trends are shown with triangles in different colors. Box plots indicate the model results (black represents GOGA; blue represents LENS). Solid triangles represent the trends significant at the 95% significance level based on P-value. Horizontal lines indicate the model mean values and vertical lines indicate the spread in each model. Black hollow circles represent the outliers.

3.4. Decomposition of AR Frequency Driven by Dynamics and Thermodynamics

By decomposing the AR frequency, we further analyze AR frequency trends driven by dynamics and thermodynamics respectively (Figure 8, 9). The spatial patterns of dynamically-driven AR frequency trends vary among seasons (Figure 8, upper), but are similar to the total trends with positive trends at the extratropics and negative trends at the subtropics (Figure 5, upper). The spatial patterns of decomposed AR frequency trends highlight the main contribution of seasonal changes in AR frequency generated by changes in large-scale atmospheric circulation (Figure 10, upper). Thermodynamically-driven AR frequency has been increasing and covered the majority

of the Southern Ocean in LENS and GOGA as ARs grow in size and intensity with increasing surface temperature. Driven by the observed SST, a cooling region near the coast of Antarctica drives decreasing AR frequency trends there which explains the more negative thermodynamically-driven AR frequency trends compared with the dynamically-driven (Figure 8 and 9, lower) and equatorward AR shifts (Figure 10, lower). The magnitudes of AR frequency trends from the GOGA ensemble mean exceed LENs ensemble mean trends (Figure 8, middle, d), indicating larger dynamic contributions driven by variation of SST, particularly during boreal winter. The seasonality of trends driven by thermodynamics is hard to identify.

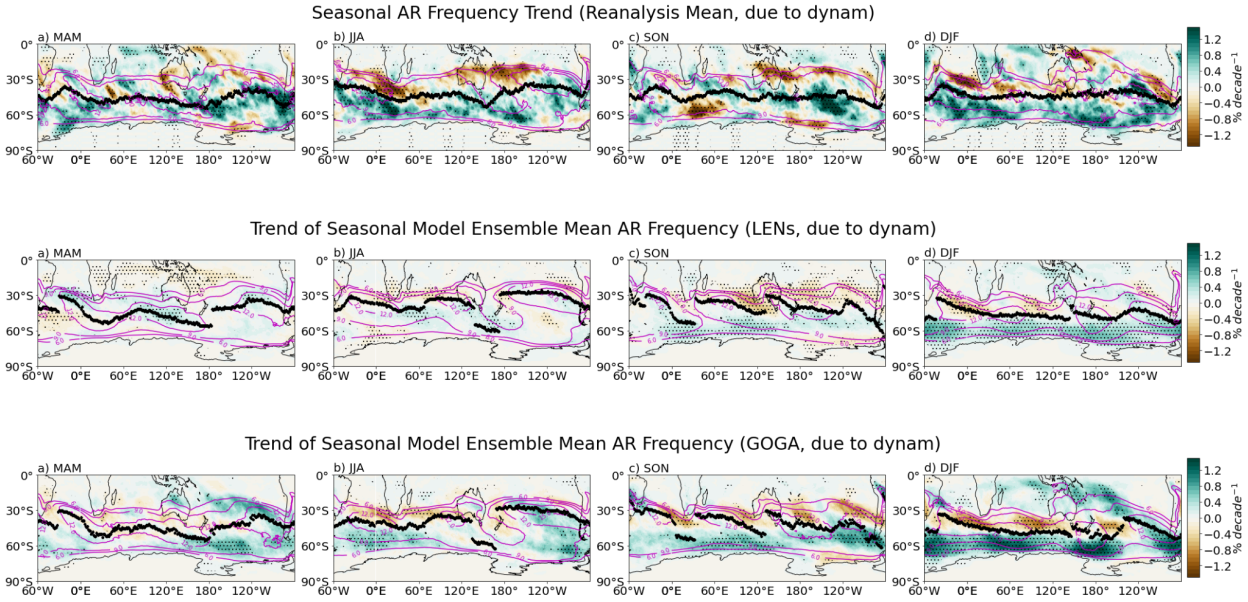

Figure 8. Spatial distribution of dynamic components of climatology (solid contours) and linear trends (shading, $\%\ decade^{-1}$): seasonal reanalysis-mean AR frequency (upper panel), seasonal AR frequency in GOGA (middle panel), seasonal AR frequency in LENS (bottom panel). Black line indicates the climatological location of peak total AR frequency. Stippling indicates regions with trends significant at the 90% significance level based on two-tailed Student's t test.

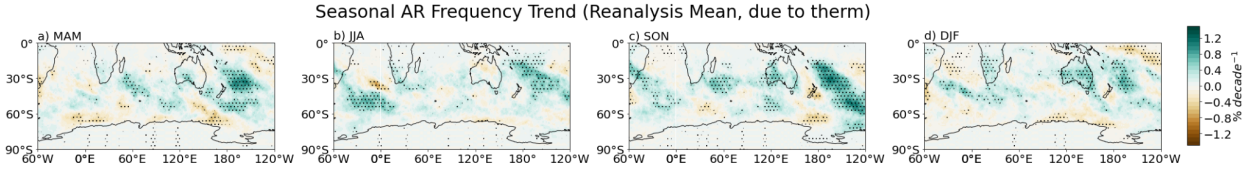

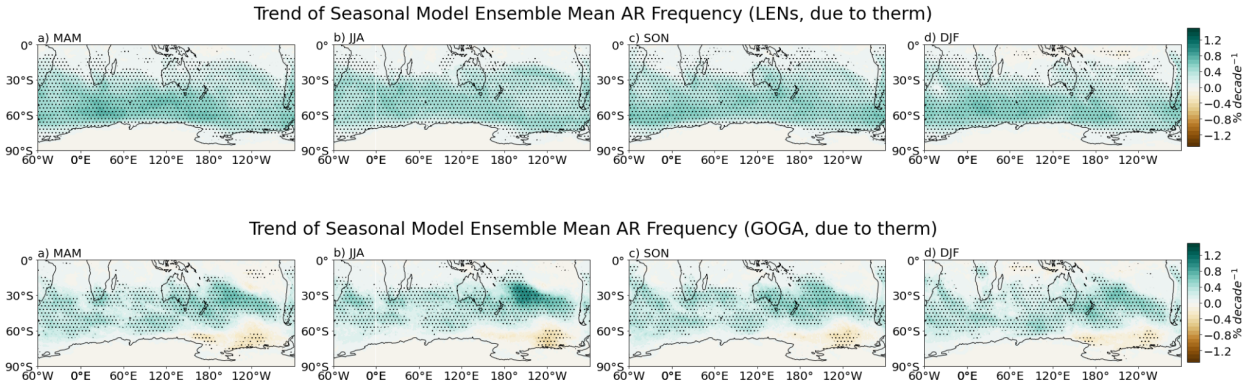

Figure 9. Spatial distribution of thermodynamic components of climatology (solid contours) and linear trends (shading, % $decade^{-1}$) of: seasonal reanalysis-mean AR frequency (upper panel), seasonal AR frequency in GOGA (middle panel), seasonal AR frequency in LENS (bottom panel). Black line indicates the climatological location of peak AR frequency. Stippling indicates regions with trends significant at the 90% significance level based on two-tailed Student's t test.

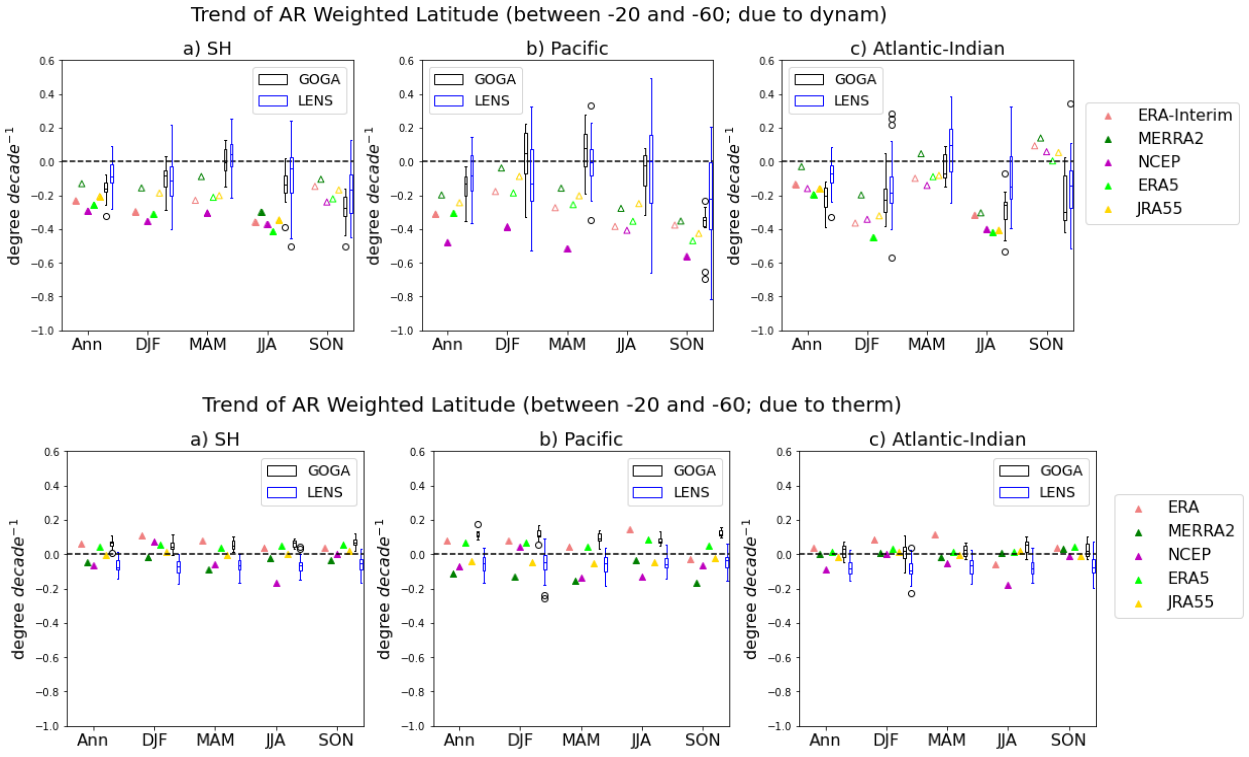

Figure 10. The linear trends of annual and seasonal AR area-weighted latitudes due to dynamic (upper panel) and thermodynamic contributions (lower panel): a) Southern Hemisphere (SH), b) Pacific Ocean basin (PA), c) Atlantic and Indian Ocean sectors (ATIN). Reanalyzed trends of AR frequency are shown with triangles in different colors. Box plots indicate the model results (black represents GOGA; blue represents LENS). Only solid triangles in the upper panel represent the trends significant at the 95% significance level based on P-value. Horizontal lines in boxes indicate the model mean values and vertical lines indicate the spread in each model. Black hollow circles are the outliers.

4. Conclusions

We analyzed the climatology and trends of ARs detected by different ARDTs over the Southern Hemisphere in observations and climate models over the past four decades of which the results are consistent with previous findings of ARTMIP. Distribution of climatology and seasonal trend of AR frequency using different ARDTs have large uncertainties. The consensus among the detection is that most high AR frequency (over 12%) concentrates within the ocean basins across mid-to-high latitudes. The distribution of observed AR frequency trends shows increased AR frequency at the extratropics resulting in the poleward AR shifts over the Southern Ocean which is further confirmed by the changes in AR locations. Detected by different AR algorithm, the annual AR frequency shifts at a rate of -0.13°±0.079°, -0.32°±0.062° and -0.018°±0.081° latitude per decade over the entire Southern Ocean (SH), Pacific (PA), and Atlantic and Indian Ocean sectors (ATIN). From the reanalyses, the annual AR shifts at a rate of -0.23°±0.077°, -0.32°±0.13° and -0.15°±0.086° latitude per decade over the entire Southern Ocean (SH), Pacific (PA), and Atlantic and Indian Ocean sectors (ATIN), in agreement with results from Ma et al. (2020). The strongest seasonal shift in the reanalyses happens in JJA at a rate of -0.38°±0.090°, -0.33°±0.12° and -0.41°±0.10° latitude per decade for SH, PA, and ATIN, and the weakest poleward shift in SON for SH at a rate of -0.16°±0.050° latitude per decade, in DJF for PA at a rate of -0.18°±0.11° latitude per decade. The AR frequency presents statistically insignificant equatorward shifts during SON over the ATIN, with the average rate of 0.20°±0.14° latitude per decade among selected ARDTs and 0.087°±0.061° latitude per decade on average in reanalyses. The intercomparison of reanalyses shows that NCEP presents the strongest signals in AR frequency trends and shifts.

The seasonality of ARs over individual ocean basins differs from each other which may indicate different climate impacts. Model results from two ensembles of CESM are used to analyze the ARs' response to anthropogenic forcing and SST variability in the Southern Hemisphere. AR frequency from LENs reveals uniform increasing pattern over the entire ocean basin under the RCP8.5 scenario. At the same time, ARs modulated by the negative IPO-like surface warming in the GOGA ensemble have reduced frequency over the cooling area near Antarctica leading to equatorward shifts over the Pacific. The pronounced equatorward shifts during DJF and MAM in GOGA deviate from the poleward AR shifts in observations. Therefore, model simulations still have potential to improve the simulation of seasonality which could relate to model's ability to simulate the atmospheric teleconnection patterns modulating the ARs (Handorf & Dethloff, 2012; Cassado & Pastor, 2012; Stoner et al., 2009).

The decomposition of AR further explains the change of ARs in another aspect. The observed AR frequency trends are mainly caused by changes in atmospheric circulation according to the dominant dynamically-driven AR frequency trends accounting for over 90% of the total trend, and also weak trends driven by thermodynamics during all the seasons. The thermodynamic effect generates increasing AR frequency over the majority of the Southern Ocean, particularly over the Pacific. Thermodynamically-driven observed AR frequency trends in reanalysis remain large uncertainties. The AR locations shift equatorward in GOGA, but poleward in LENs which could be explained by reconciled trends due to observed SST anomalies.

Data Availability Statement

ERA-Interim and ERA5 data can be found from ECMWF (https://apps.ecmwf.int/datasets/data/interim-full-daily/levtype=sfc/;https://www.ecmwf.int/en/fo

recasts/dataset/ecmwf-reanalysis-v5). MERRA2 data is available at MDISC, managed by the NASA Goddard Earth Sciences (GES) Data and Information Services Center (DISC) (https://disc.gsfc.nasa.gov/datasets?project=MERRA-2). NCEP data can be found online (https://psl.noaa.gov/data/gridded/data.ncep.reanalysis.html). JRA55 research data is archived at the National Center for Atmospheric Research, Computational and Informaiton Systems Laboratory. Data from CESM large ensemble are available online (http://www.cesm.ucar.edu/projects/community-jects/LENS/data-sets.html). GOGA 10-member ensemble (ERSSTv4) are available online (http://www.cesm.ucar.edu/experiments/cesm1.1/LE/). Details about Atmospheric Rivers Tracking Methods Intercomparison Project (ARTMIP) can be found on their official website (https://www.cgd.ucar.edu/projects/artmip).

References

Allan, R. P. The role of water vapour in earth's energy flows. Surv. Geophys. 33, 557–564 (2012).

Algarra, I., Nieto, R., Ramos, A.M. *et al.* Significant increase of global anomalous moisture uptake feeding landfalling Atmospheric Rivers. *Nat Commun* 11, 5082 (2020). https://doi.org/10.1038/s41467-020-18876-w

Benedict, J. J., Clement, A. C., & Medeiros, B. (2019). Atmospheric blocking and other large‐scale precursor patterns of land falling atmospheric rivers in the North Pacific: A CESM2 study. Journal of Geophysical Research: Atmospheres, 124, 11,330–11,353. https://doi.org/10.1029/2019JD030790

Boisier, J. P., Rondanelli, R., Garreaud, R. D., and Muñoz, F. (2016), Anthropogenic and natural contributions to the Southeast Pacific precipitation decline and recent megadrought in central Chile, *Geophys. Res. Lett.*, 43, 413– 421, doi:10.1002/2015GL067265.

Casado, M.J., Pastor, M.A. Use of variability modes to evaluate AR4 climate models over the Euro-Atlantic region. Clim Dyn 38, 225–237 (2012). https://doi.org/10.1007/s00382-011-1077-2

Chen, G., & Held, I. M. (2007). Phase speed spectra and the recent poleward shift of Southern Hemisphere surface westerlies. Geophysical Research Letters, 34, L21805. https://doi.org/10.1029/2007GL031200

Collow, A.B., Shields, C.A., Guan, B., Kim, S., Lora, J.M., McClenny, E.E., Nardi, K., Payne, A., Reid, K., Shearer, E. J. , Tome, R., Wille, J.D., Ramos, A.M., Gorodetskaya, I.V., Leung, L.R., O'Brien, T.A., Ralph, F.M., Rutz, J. Ullirich, P.A., Wehner, M., (2022) An Overview of ARTMIP's Tier 2 Reanalysis Intercomparison: Uncertainty in the Detection of Atmospheric Rivers and their Associated Precipitation, Journal of Geophysical Research, Atmospheres, https://agupubs.onlinelibrary.wiley.com/doi/10.1029/2021JD036155.

Davison, B.J., Hogg, A.E., Rigby, R. *et al.* Sea level rise from West Antarctic mass loss significantly modified by large snowfall anomalies. *Nat Commun* 14, 1479 (2023). https://doi.org/10.1038/s41467-023-36990-3

Dettinger, M.D.; Ralph, F.M.; Das, T.; Neiman, P.J.; Cayan, D.R. Atmospheric Rivers, Floods and the Water Resources of California. *Water* **2011**, *3*, 445-478. https://doi.org/10.3390/w3020445

DÖRTHE Handorf & KLAUS Dethloff (2012) How well do state-of-the-art atmosphere-ocean general circulation models reproduce atmospheric teleconnection patterns?, Tellus A: Dynamic Meteorology and Oceanography, 64:1, DOI: 10.3402/tellusa.v64i0.19777

Francis, D., Mattingly, K. S., Temimi, M., Massom, R., & Heil, P. (2020). On the crucial role of atmospheric rivers in the two major Weddell
Polynya events in 1973 and 2017 in Antarctica. *Science Advances*, *6*(46), eabc2695. https://doi.org/10.1126/sciadv.abc2695

Fish, M. A., Wilson, A. M. & Raph, F. M. Atmospheric river families: definition and associated synoptic conditions. *J. Hydrometeorol.* **20**, 2091–2108 (2019).

Gershunov, A., Shulinga, T., Ralph, F. M., Lavers, D. A., & Rutz, J. J. (2017). Assessing the climate-scale variability of atmospheric rivers affecting western North America. *Geophysical Research Letters*, *44*, 7900–7908. https://doi.org/10.1002/2017GL074175

Guan, B., & Waliser, D. E. (2015). Detection of atmospheric rivers: Evaluation and application of an algorithm for global studies. Journal of Geophysical Research: Atmospheres, 120, 12,514–12,535. https://doi.org/10.1002/2015JD024257

Guan, B., Molotch, N. P., Waliser, D. E., Fetzer, E. J., & Neiman, P. J. (2010). Extreme snowfall events linked to atmospheric rivers and surface air temperature via satellite measurements. *Geophysical Research Letters*, *37*, L20401. https://doi.org/10.1029/2010GL044696

Gonzales, K. R., Swain, D. L., Barnes, E. A., & Diffenbaugh, N. S. (2020). Moisture‐versus wind‐dominated flavors of atmospheric rivers. Geophysical Research Letters, 47, e2020GL090042. https://doi.org/10.1029/2020GL090042

Huang, X., Swain, D. L., & Hall, A. D. (2020). Future precipitation increase from very high resolution ensemble downscaling of extreme atmospheric river storms in California. Science Advances, 6, eaba1323. https://doi.org/10.1126/sciadv.aba1323

Hegyi, B. M. & Taylor, P. C. The unprecedented 2016–2017 Arctic sea ice growth season: the crucial role of atmospheric rivers and longwave fluxes. *Geophys. Res. Lett.* **45**, 5204–5212 (2018).

Ignacio Fuentes, Rodrigo Fuster, David Avilés & Willem Vervoort (2021) Water scarcity in central Chile: the effect of climate and land cover changes on hydrologic resources, Hydrological Sciences Journal, 66:6, 1028-1044, DOI: 10.1080/02626667.2021.1903475

Komatsu, K. K., Alexeev, V. A., Repina, I. A. & Tachibana, Y. Poleward upgliding Siberian atmospheric rivers over sea ice heat up arctic upper air. *Sci. Rep.* **8**, 2872 (2018)

Kushner, P. J., I. M. Held, and T. L. Delworth, 2001: Southern Hemisphere Atmospheric Circulation Response to Global Warming. *J. Climate*, **14**, 2238–2249, https://doi.org/10.1175/1520-0442(2001)014<0001:SHACRT>2.0.CO;2.

Lora, J. M., Shields, C. A., & Rutz, J. J. (2020). Consensus and disagreement in atmospheric river detection: ARTMIP global catalogues.*Geophysical Research Letters*, *47*, e2020GL089302. https://doi.org/10.1029/2020GL089302

Lora, J. M., Mitchell, J. L., Risi, C., and Tripati, A. E. (2017), North Pacific atmospheric rivers and their influence on western North America at the Last Glacial Maximum, *Geophys. Res. Lett.*, 44, 1051– 1059, doi:10.1002/2016GL071541.

Ma, W., Chen, G., & Guan, B. (2020). Poleward shift of atmospheric rivers in the Southern Hemisphere in recent decades. Geophysical Research Letters, 47, e2020GL089934. https://doi.org/10.1029/2020GL089934

Maclennan, M. L., Lenaerts, J. T. M., Shields, C., & Wille, J. D. (2022). Contribution of atmospheric rivers to Antarctic precipitation. *Geophysical Research Letters*, *49*, e2022GL100585. https://doi.org/10.1029/2022GL100585

McClenny, E. E., Ullrich, P. A., & Grotjahn, R. (2020). Sensitivity of atmospheric river vapor transport and precipitation to uniform sea surface temperature increases. *Journal of Geophysical Research: Atmospheres*, *125*. https://doi.org/10.1029/2020jd033421

McKay, R. C., Boschat, G., Rudeva, I., Pepler, A., Purich, A., Dowdy, A., Hope, P., Gillett, Z. E., & Rauniyar, S.(2023). Can southern Australian rainfall decline be explained? A review of possible drivers. *WIREs Climate Change*, 14(2), e820. https://doi.org/10.1002/wcc.820

Michaelis, A. C., Gershunov, A., Weyant, A., Fish, M. A., Shulgina, T., & Ralph, F. M. (2022). Atmospheric river precipitation enhanced by climate change: A case study of the storm that contributed to California's Oroville Dam crisis. Earth's Future, 10, e2021EF002537. https://doi.org/10.1029/2021EF002537

Mundhenk, B. D., Barnes, E. A., Maloney, E. D., & Nardi, K. M. (2016). Modulation of atmospheric rivers near Alaska and the U.S. West Coast by northeast Pacific height anomalies. Journal of Geophysical Research: Atmospheres, 121, 12,751–12,765. https://doi.org/10.1002/2016JD025350

Mundhenk, B. D., E. A. Barnes, and E. D. Maloney, 2016: All-Season Climatology and Variability of Atmospheric River Frequencies over the North Pacific. *J. Climate*, **29**, 4885–4903, https://doi.org/10.1175/JCLI-D-15-0655.1.

Nash, D., Waliser, D., Guan, B., Ye, H. & Ralph, F. M. The role of atmospheric rivers in extratropical and polar hydroclimate. *J. Geophys. Res. Atmos.* **123**, 6804–6821 (2018).

Neiman, P. J., Ralph, F. M., Wick, G. A., Lundquist, J. D., & Dettinger, M. D. (2008). Meteorological characteristics and overland precipitation impacts of atmospheric rivers affecting the west coast of North America based on eight years of SSM/I satellite observations. Journal of Hydrometeorology, 9(1), 22–47. https://doi.org/10.1175/2007jhm855.1

O'Brien, T. A., Risser, M. D., Loring, B., Elbashandy, A. A., Krishnan, H., Johnson, J., Patricola, C. M., O'Brien, J. P., Mahesh, A., Prabhat, Arriaga Ramirez, S., Rhoades, A. M., Charn, A., Inda Díaz, H., and Collins, W. D.: Detection of atmospheric rivers with inline uncertainty quantification: TECA-BARD v1.0.1, Geosci. Model Dev., 13, 6131–6148, https://doi.org/10.5194/gmd-13-6131-2020, 2020.

O'Brien, T. A., Wehner, M. F., Payne, A. E., Shields, C. A., Rutz, J. J., Leung, L.-R., et al. (2022). Increases in future AR count and size: Overview of the ARTMIP Tier 2 CMIP5/6 experiment. Journal of Geophysical Research: Atmospheres, 127, e2021JD036013. https://doi.org/10.1029/2021JD036013

O'Brien, T. A., and Coauthors, 2020: Detection Uncertainty Matters for Understanding Atmospheric Rivers. Bull. Amer. Meteor. Soc., 101, E790–E796, https://doi.org/10.1175/BAMS-D-19-0348.1.

O'Gorman, P. A. & Muller, C. J. How closely do changes in surface and column water vapor follow Clausius-Clapeyron scaling in climate change simulations? Environ. Res. Lett. 5, 1–7 (2010).

Pan, M., & Lu, M. (2020). East Asia Atmospheric River catalog: Annual cycle, transition mechanism, and precipitation. *Geophysical Research Letters*, 47, e2020GL089477. https://doi.org/10.1029/2020GL089477

Pan, M., & Lu, M. (2019). A novel atmospheric river identification algorithm. *Water Resources Research*, 55, 6069– 6087. https://doi.org/10.1029/2018WR024407

Payne, A.E., Demory, ME., Leung, L.R. et al. Responses and impacts of atmospheric rivers to climate change. Nat Rev Earth Environ 1, 143–157 (2020). https://doi.org/10.1038/s43017-020-0030-5

Payne, A. E., & Magnusdottir, G. (2014). Dynamics of landfalling atmospheric rivers over the North Pacific in 30 years of MERRA reanalysis. Journal of Climate, 27(18), 7133–7150. https://doi.org/10.1175/jcli-d-14-00034.1

Prabhat, Kashinath, K., Mudigonda, M., Kim, S., Kapp-Schwoerer, L., Graubner, A., Karaismailoglu, E., von Kleist, L., Kurth, T., Greiner, A., Mahesh, A., Yang, K., Lewis, C., Chen, J., Lou, A., Chandran, S., Toms, B., Chapman, W., Dagon, K., Shields, C. A., O'Brien, T., Wehner, M., and Collins, W.: ClimateNet: an expert-labeled open dataset and deep learning architecture for enabling high-precision analyses of extreme weather, Geosci. Model Dev., 14, 107–124, https://doi.org/10.5194/gmd-14-107-2021, 2021.

Reid, K. J., King, A. D., Lane, T. P., & Short, E. (2020). The sensitivity of atmospheric river identification to integrated water vapor transport threshold, resolution, and regridding method. *Journal of Geophysical Research: Atmospheres*, *125*. https://doi.org/10.1029/2020jd032897

Rutz, J. J., Steenburgh, W. J., & Ralph, F. M. (2014). Climatological characteristics of atmospheric rivers and their inland penetration over the western United States. Monthly Weather Review, 142, 905–921. https://doi.org/10.1175/MWR-D-13-00168.1

Shaw, T. A., Baldwin, M., Barnes, E. A., Caballero, R., Garfinkel, C. I., Hwang, Y.-T., et al. (2016). Storm track processes and the opposing influences of climate change. *Nature Geoscience*, *9*, 656–664.

Shields, C. A., Payne, A. E., Shearer, E. J., Wehner, M. F., O'Brien, T. A., Rutz, J. J., et al. (2023). Future atmospheric rivers and impacts on precipitation: Overview of the ARTMIP Tier 2 high-resolution global warming experiment. Geophysical Research Letters, 50, e2022GL102091. https://doi.org/10.1029/2022GL102091

Shields, C. A., J. J. Rutz, L. R. Leung, F. M. Ralph, M. Wehner, T. O'Brien, and R. Pierce, 2019: Defining Uncertainties through Comparison of Atmospheric River Tracking Methods. Bull. Amer. Meteor. Soc., 100, ES93–ES96, https://doi.org/10.1175/BAMS-D-18-0200.1.

Shields, C. A., Rutz, J. J., Leung, L.-Y., Ralph, F. M., Wehner, M., Kawzenuk, B., Lora, J. M., McClenny, E., Osborne, T., Payne, A. E., Ullrich, P., Gershunov, A., Goldenson, N., Guan, B., Qian, Y., Ramos, A. M., Sarangi, C., Sellars, S., Gorodetskaya, I., Kashinath, K., Kurlin, V., Mahoney, K., Muszynski, G., Pierce, R., Subramanian, A. C., Tome, R., Waliser, D., Walton, D., Wick, G., Wilson, A., Lavers, D., Prabhat, Collow, A., Krishnan, H., Magnusdottir, G., and Nguyen, P.: Atmospheric River Tracking Method Intercomparison Project (ARTMIP): project goals and experimental design, Geosci. Model Dev., 11, 2455–2474, https://doi.org/10.5194/gmd-11-2455-2018, 2018.

Stoner, A. M. K., K. Hayhoe, and D. J. Wuebbles, 2009: Assessing General Circulation Model Simulations of Atmospheric Teleconnection Patterns. J. Climate, 22, 4348–4372, https://doi.org/10.1175/2009JCLI2577.1.

Swart, N. C., J. C. Fyfe, N. Gillett, and G. J. Marshall, 2015: Comparing Trends in the Southern Annular Mode and Surface Westerly Jet. *J. Climate*, **28**, 8840–8859, https://doi.org/10.1175/JCLI-D-15-0334.1.

Swain, D. L., Langenbrunner, B., Neelin, J. D., & Hall, A. (2018). Increasing precipitation volatility in twenty-first century California. *Nature Climate Change*, *8*, 427–433. https://doi.org/10.1038/s41558-018-0140-y

Solman, S. A., and I. Orlanski, 2014: Poleward Shift and Change of Frontal Activity in the Southern Hemisphere over the Last 40 Years. *J. Atmos. Sci.*, **71**, 539–552, https://doi.org/10.1175/JAS-D-13-0105.1.

Thomas, J. L., Waugh, D. W., and Gnanadesikan, A. (2015), Southern Hemisphere extratropical circulation: Recent trends and natural variability, Geophys. Res. Lett., 42, 5508–5515, doi:10.1002/2015GL064521.

Turner, J., Phillips, T., Thamban, M., Rahaman, W., Marshall, G. J., Wille, J. D., et al. (2019). The dominant role of extreme precipitation events in Antarctic snowfall variability. *Geophysical Research Letters*. *46*, 3502–3511. https://doi.org/10.1029/2018GL081517

Ullrich, P. A., & Zarzycki, C. M. (2017). Tempest Extremes: A framework for scale-insensitive pointwise feature tracking on unstructured grids. *Geoscientific Model Development*, *10*(3), 1069–1090. https://doi.org/10.5194/gmd-10-1069-2017

Waugh, D. W., Banerjee, A., Fyfe, J. C., & Polvani, L. M. (2020). Contrasting recent trends in Southern Hemisphere westerlies across different ocean basin. Geophysical Research Letters, 47, e2020GL088890. https://doi.org/10.1029/2020GL088890

Wille, J. D., Favier, V., Gorodetskaya, I. V., Agosta, C., Kittel, C., Beeman, J. C., et al. (2021). Antarctic atmospheric river climatology and precipitation impacts. *Journal of Geophysical Research: Atmospheres*, *126*, e2020JD033788. https://doi.org/10.1029/2020JD033788

Wille, J.D., Favier, V., Dufour, A. *et al.* West Antarctic surface melt triggered by atmospheric rivers. *Nat. Geosci.* 12, 911–916 (2019). https://doi.org/10.1038/s41561-019-0460-1

Waliser, D., Guan, B. Extreme winds and precipitation during landfall of atmospheric rivers. *Nature Geosci* **10**, 179–183 (2017). https://doi.org/10.1038/ngeo2894

Yang, D., Arblaster, J. M., Meehl, G. A., England, M. H., Lim, E.‐P., Bates, S., & Rosenbloom, N. (2020). Role of tropical variability in driving decadal shifts in the Southern Hemisphere summertime eddy‐driven jet. Journal of Climate, 33, 5445–5463. https://doi.org/10.1175/jcli‐d‐19‐0604.1

Zhang, Z., Ralph, F. M., & Zheng, M. (2019). The relationship between extratropical cyclone strength and atmospheric river intensity and position. Geophysical Research Letters, 46, 1814–1823. https://doi.org/10.1029/2018GL079071

Zhou, Y., O'Brien, T. A., Ullrich, P. A., Collins, W. D., Patricola, C. M., & Rhoades, A. M. (2021). Uncertainties in atmospheric river lifecycles by detection algorithms: Climatology and variability. Journal of Geophysical Research: Atmospheres, 126, e2020JD033711. https://doi.org/10.1029/2020JD033711.

Zhu, Y., and R. E. Newell, 1998: A Proposed Algorithm for Moisture Fluxes from Atmospheric Rivers. Mon. Wea. Rev., 126, 725–735, https://doi.org/10.1175/1520-0493(1998)126<0725:APAFMF>2.0.CO;2